ORIGINAL ARTICLE

An extensive record of orogenesis recorded in a Madagascar granulite

Forrest Horton[1] 🆔 | Robert M. Holder[2] 🆔 | Carl R. Swindle[3]

[1]Geology and Geophysics Department, Woods Hole Oceanographic Institution, Woods Hole, Massachusetts, USA

[2]Earth and Environmental Sciences Department, University of Michigan, Ann Arbor, Michigan, USA

[3]Division of Geological and Planetary Sciences, California Institute of Technology, Pasadena, California, USA

Correspondence

Forrest Horton, Geology and Geophysics Department, Woods Hole Oceanographic Institution, Woods Hole, MA 02543, USA.
Email: fhorton@whoi.edu

Robert M. Holder, Earth and Environmental Sciences Department, University of Michigan, Ann Arbor, MI 48109-1005 USA.
Email: roholder@umich.edu

Abstract

We present a comprehensive petrological and geochronological study of a single granulite sample from the lithosphere-scale Beraketa shear zone in southern Madagascar to constrain the orogenic history of Gondwana assembly in this region. The studied sample provides a panoply of data constraining the pro-grade, retrograde, and late metasomatic history of the region via the application of Ti-in-quartz, Ti-in-zircon, Zr-in-rutile, and Al-in-orthopyroxene thermobarometry; phase-equilibrium modelling; U–Pb monazite, zircon, and rutile petrochronology; and trace element diffusion chronometry in rutile. Our results reveal five stages of metamorphism along a narrow clockwise P–T path that may have begun as early as 620–600 Ma and certainly by 580–560 Ma, based on the oldest concordant zircon dates. The rock was heated to >725°C at less than 7.5 kbar (Stage 1) before burial to ∼8 kbar (Stage 2). By c. 540 Ma, the rock had heated to ∼970°C at ∼9 kbar, and lost approximately 12% melt (Stage 3), before decompressing and cooling to the solidus at ∼860°C and 6.5 kbar within 10 Ma (Stage 4). The vast majority of monazite and zircon dates record Stage 4 cooling and exhumation. Monazite and zircon rim dates as young as c. 510 Ma record subsolidus cooling (Stage 5) and associated symplectite formation around garnet. U–Pb rutile dates record partial resetting at c. 460 Ma; Zr- and Nb-in-rutile diffusion chronometry link these dates to a metasomatic event that lasted <1 Ma at ∼600°C. In addition to chronicling a near-complete cycle of metamorphism in southern Madagascar, this study constrains the rates of heating and cooling. We estimate that heating (7–14°C/Ma) outpaced reasonable radiogenic heating rates with modest mantle heat conduction. Therefore, we conclude that elevated mantle heat conduction or injection of mantle-derived magmas likely contributed to regional ultrahigh-temperature metamorphism (UHTM). Exhumation and cooling from peak metamorphic conditions to the solidus occurred at rates greater than 0.45 km/Ma and 14°C/Ma.

KEYWORDS

granulite, lithosphere-scale shear zone, petrochronology, ultrahigh-temperature metamorphism

F. Horton and R. M. Holder contributed equally to this work.

Some of this work was carried out in the Earth Sciences Department at University of California Santa Barbara, Santa Barbara, CA 93106, USA.

1 | INTRODUCTION

Extreme heating of continental crust can influence the tectonic evolution of orogens (Beaumont et al., 2004; Gerya et al., 2008; Lexa et al., 2011) and control the geochemical modification of crust (Clemens & Vielzeuf, 1987; Taylor & McLennan, 1995). Yet high-temperature processes are often obscured in the rock record by partial melting, diffusion, and retrogression. In granulite terranes, reconstructing pressure–temperature–time ($P–T–t$) histories often requires synthesizing data from many samples that record different segments of the $P–T–t$ path (e.g., Boger et al., 2012; Holder, Hacker, et al., 2018; Jöns & Schenk, 2011). This approach is limited by the assumption that all samples—often collected across tens to hundreds of kilometers in highly deformed terranes—experienced similar $P–T–t$ conditions.

In this study, we overcome many of these challenges by performing a detailed analysis of a single granulite sample from southern Madagascar that retains a uniquely complete record of Pan-African orogenesis (Pan-African referring here to the combined influences of the proposed East African, Kuunga, and Malagasy orogenies in southern Madagascar). The sample is a garnet–cordierite–orthopyroxene migmatitic gneiss exhibiting diagnostic evidence for mineral reactions along with a diverse accessory mineral assemblage that lends itself to informative petrochronology (e.g., Clark et al., 2019). We were able to distinguish prograde, peak, and retrograde mineral growth by linking mineral reaction textures with equilibrium thermodynamic models. By integrating these observations with multimineral U–Pb petrochronology (zircon, monazite, and rutile) and 4^+ cation thermometry (zircon, rutile, and quartz), we were able to quantitatively reconstruct the $P–T–t$ trajectory and test previously proposed hypotheses for the formation of regional (ultra)high-temperature metamorphism. Consequently, this single granulite sample provides a nuanced record of regional orogenesis that compliments terrane-scale petrological studies (e.g., Boger et al., 2012; Giese et al., 2011; Holder, Hacker, et al., 2018; Horton et al., 2016; Jöns & Schenk, 2011) and exemplifies the power and reach of recent analytical and computational advances. Our results also highlight the complexity of granulite formation and modification—processes that often leave only cryptic records in high-temperature rocks.

2 | BACKGROUND

The Neoproterozoic collision between East Gondwana (India, Antarctica, and Australia) and West Gondwana (Africa and South America) amalgamated oceanic arcs, microcontinents, and intervening sedimentary basins into an extensive collisional orogen (Boger et al., 2014, 2015, 2019; Collins et al., 2012; Fitzsimons, 2016; Fritz et al., 2013; Stern, 1994; Tucker et al., 2014). The midcrustal section of this orogen exposed in southern Madagascar includes a broad zone (>20,000 km^2) that underwent high-temperature metamorphism to ultrahigh-temperature metamorphism (UHTM) (GAF-BGR, 2008; Horton et al., 2016; Jöns & Schenk, 2011; Martelat et al., 2012). UHTM occurred almost exclusively in what is referred to as the Anosyen domain (Figure 1), which mostly consists of aluminous metasediments, calc-silicate gneisses, and felsic metavolcanosedimentary units (GAF-BGR, 2008). The main collisional orogeny in southern Madagascar began at c. 585 Ma and lasted until c. 525 Ma (Holder, Hacker, et al., 2018; Horton et al., 2016; Martelat et al., 2000; Tucker et al., 2014). The southern Anosyen domain reached peak conditions of 900–1000°C at 6–10 kbar (Boger et al., 2012; Holder & Hacker, 2019; Holder, Hacker, et al., 2018; Holder, Sharp, & Hacker, 2018; Horton et al., 2016; Jöns & Schenk, 2011). Peak temperatures were slightly lower to the west (Markl et al., 2000; Martelat et al., 1997) and north (Boger et al., 2012; Horton et al., 2016; Jöns & Schenk, 2011; Raith et al., 2008; although, see Martelat et al., 2012) and were lower still (≤800°C) in the Ikalamavony fold-thrust belt to the north–northeast (Ganne et al., 2014; Grégoire et al., 2009; Holder & Hacker, 2019). See Figure S1 for a compilation of previous $P–T$ estimates.

Southern Madagascar bedrock exhibits polyphase granulite facies fabrics. Early structures include recumbent folds and stretching lineations attributable to E–W shortening (de Wit et al., 2001; Martelat et al., 2000). Distributed deformation gradually converged into near-vertical, 15–25 km wide, N-S trending shear zones. The sample investigated in this study (F2910B) is from the southern portion of the ~400-km-long N-S trending Berakета shear zone, which separates the Androyen and Anosyen domains (Figure 1). We collected the rock from the active Ampandrandava phlogopite mine (Martin et al., 2014) near where Jöns and Schenk (2011) collected their sample MD-89. Thermobarometry by Jöns and Schenk (2011) suggested that conditions reached approximately 1000°C and 9 kbar. Our previous work on sample F2910B—referred to as 10B1 in Horton et al. (2016)—hinted that it contained an invaluable record of orogenesis: concordant U–Pb zircon dates span the main stage of orogenesis (570–515 Ma) and trace element thermometry indicates it experienced UHTM (Horton et al., 2016).

Heating mechanisms responsible for UHTM remain controversial (Clark et al., 2011; Kelsey & Hand, 2015),

FIGURE 1 Bedrock geology map of southern Madagascar (modified from Horton et al., 2016). Sample F2910B is from the Beraketa shear zone between the Anosyen and Androyen domains. Dashed grey lines are metamorphic isotherms based on 4^+ cation thermometry and mineral assemblages. Patterned areas along tectonic domain boundaries approximate the extent of focused deformation in major shear zones
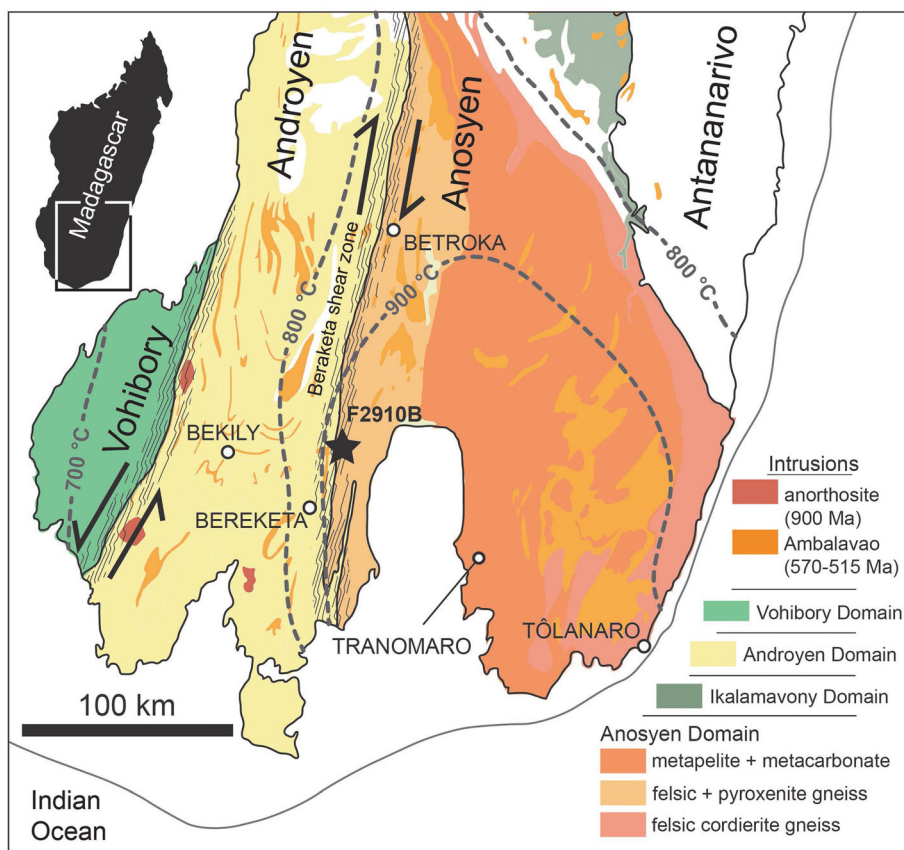
particularly in Madagascar (Holder, Hacker, et al., 2018; Horton et al., 2016). There, high concentrations of U, Th, and K are correlated with metamorphic grade, suggesting that radiogenic heating was a primary driver of regional (U)HTM (Horton et al., 2016). However, low pressures (≤6.5 kbar) estimated for UHTM in the Anosyen domain (e.g., Boger et al., 2012; Holder, Hacker, et al., 2018) and a relatively short duration (≤20 Ma) of UHTM within the broader orogenic cycle have led to the hypothesis that additional heat sources played a role (Holder, Hacker, et al., 2018). Other potential heating mechanisms include the injection of mantle-derived magmas (Holder, Hacker, et al., 2018; Jöns & Schenk, 2011) or elevated heat flow at the base of the crust resulting from a thinned mantle lithosphere (Holder, Hacker, et al., 2018; Horton et al., 2016); the latter hypothesis is consistent with the interpretation of southern Madagascar terranes as a series of microcontinental arcs or outer continental margin sedimentary sequences (e.g., Boger et al., 2012, 2019).

3 | SAMPLE DESCRIPTION

F2910B is a cordierite–biotite–quartz–garnet–plagioclase–orthopyroxene gneiss (modal abundances are listed in Table 1) containing minor ilmenite, rutile, monazite, and zircon (Figure 2a). The matrix of the rock is composed of xenoblastic and approximately equant garnet and orthopyroxene (1–4 mm in diameter). Plagioclase (which lacks exsolution lamellae) and quartz are xenoblastic, irregularly shaped, and typically ≤1.5 mm across; these minerals are mainly interstitial to orthopyroxene and garnet, but also exist together in larger segregations (∼6 mm across). Garnet is always separated from quartz by double-layered coronae of orthopyroxene (adjacent to quartz) and plagioclase (adjacent to garnet). Garnet is locally mantled by symplectites of orthopyroxene and cordierite (Figure 2b), some of which also contain minor biotite (Figure 2c). Outside of these symplectites, cordierite and biotite (10–1000 μm) occur in intimate association with, and often mantle, orthopyroxene. Biotite occurs as rare inclusions in garnet and orthopyroxene. A single large (∼0.5 × 1 mm) cordierite inclusion was observed in garnet (Figure 2c). Although this is an isolated example, the cordierite grain appears to be a legitimate inclusion, rather than an artefact of thin sectioning, due to the absence of biotite or orthopyroxene (which are consistently associated with cordierite elsewhere) and the prominent set of radial fractures in the host garnet surrounding the inclusion. No

TABLE 1 Mineral modes in thin section

	Mineral						
	Plagioclase	Cordierite	Biotite	Garnet	Quartz	Orthopyroxene	Ilmenite+rutile
Mode	30.10	5.00	8.00	10.90	9.20	35.50	1.50
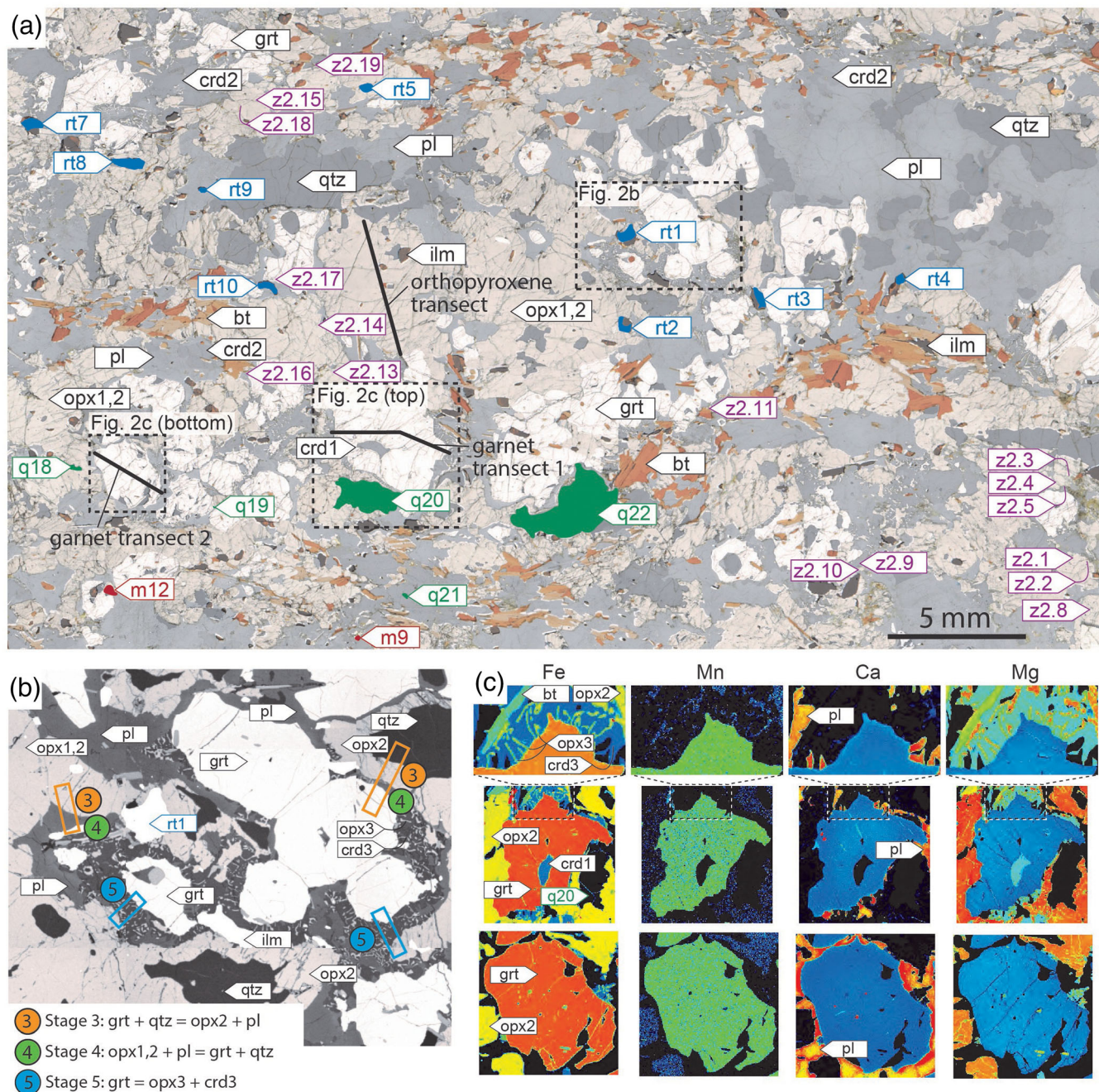
FIGURE 2 Mineral reaction textures for sample F2910B. (a) Composite backscatter electron and natural light mosaic of a thin section. Numbers denote minerals analysed by laser ablation split-stream (LASS) and electron microprobe analysis (EMPA) (note that many analyses were done on a second thin section). (b) Backscattered-electron image showing retrograde textures. (c) EMPA maps of garnet reaction textures. Note that the upper garnet is rotated 90° counterclockwise, relative to (a). Analysed mineral grains are labelled (m, monazite; rt, rutile; q, quartz; z, zircon) and numbered. Otherwise, generic mineral abbreviations are used (bt, biotite; crd, cordierite; g, garnet; ilm, imenite; opx, orthopyroxene; qtz, quartz) and numbered by generation

inclusions of orthopyroxene in garnet, or vice versa, were observed.

Monazite grains are 150–300 μm in diameter and spatially associated with biotite and cordierite. Zircon grains exist in, and are adjacent to, every major mineral phase. Most are 30–40 μm across, subhedral, and have dark sector-zoned rims in cathodoluminescence images. Some zircon grains contain CL-bright, fractured cores with embayments. Several larger zircon grains (50–100 μm) are attached to—and appear to have grown from—rutile. Exsolution-free rutile and ilmenite exist in isolation and together, both in the matrix and as inclusions in garnet and orthopyroxene.

4 | METHODS

4.1 | Electron microprobe analysis

We measured the compositions of each major phase in thin sections using a Cameca SX-100 electron probe microanalyser at University of California Santa Barbara. We calculated an effective bulk composition for the rock from mineral compositions (Table S1), modes (Table 1), and molar volumes. We also mapped La, Y, U, and Th zoning in six monazite grains using a 1-μm step size. For thermometry, we measured Ti in 10 quartz grains (three to 10 analyses per grain). Using a JEOL JXA-8200 electron microprobe analysis (EMPA) at California Institute of Technology, we measured Zr along rim-to-rim transects across 14 rutile grains (∼40 analyses per grain). To supplement these results, we also measured Zr and Nb along a core-to-rim transect with 3- to 4-μm spacing in one rutile with diffusive zoning (rt4).

4.2 | Phase-equilibrium modelling

To calculate equilibrium assemblage phase diagrams, we used Theriak-Domino (compiled by D. K. Tinkham and downloaded from http://www.dtinkham.net/peq.html on 8 February 2019), the end-member thermodynamic data of Holland and Powell (2011), and the solution models of White, Powell, Holland, et al. (2014); White, Powell, and Johnson (2014). The proportion of ferric iron was estimated to be 10 at.% ($Fe^{3+}/Fe^{total} = 0.1$), because lower values are inconsistent with the coexistence of rutile and ilmenite in the matrix and as inclusions in garnet and orthopyroxene; much higher values are probably unreasonable as well, given the lack of magnetite observed in the rock. Reasonable variations in model ferric iron content (0–20 at.%) for ilmenite-bearing rocks were tested and found to have little influence on the

calculated phase equilibria for this rock beyond the limited range of pressure and temperature over which ilmenite and rutile were both stable.

For the purposes of phase-equilibrium modelling, the rock was assumed to be fluid-undersaturated during granulite facies metamorphism. The H_2O content used for our modelling (0.97 wt%) was calculated from the mode of biotite. We infer that F2910B had melt extracted during heating through the granulite facies, based on the preservation of its residual granulite-facies mineral assemblage (Spear et al., 1999; White & Powell, 2002). To calculate plausible prograde phase assemblages (prior to melt extraction), we reintegrated melt into the whole-rock composition following the method of White et al. (2004) and Korhonen et al. (2013). Two steps of melt reintegration (addition of ∼12 vol.% melt total) were required to saturate the model with H_2O at the solidus. Despite H_2O saturation, orthopyroxene was calculated to be stable below the solidus, which is likely an artefact of the calculation, due to the absence of an appropriate orthoamphibole activity-composition model. We do not attempt to interpret subsolidus metamorphism for this sample. For critical assessment of different approaches to melt reintegration, see Bartoli (2017).

4.3 | Al-in-orthopyroxene thermobarometry

We used the RCLC (an abbreviation for 'recalculation') thermobarometry method (Chacko, 1996; Pattison et al., 2003; Pattison et al., 2019) to calculate peak P–T conditions based on Al solubility in orthopyroxene and corrected for retrograde Fe–Mg exchange among minerals. Mineral analyses used in the calculations were chosen from near-homogeneous portions of grain interiors, as identified in EMPA transects (Figure S4a–c). Five analyses each of garnet, orthopyroxene, and plagioclase were selected and P–T estimates were made for all possible combinations of these analyses ($n = 125$ calculations) to assess the sensitivity of the results to minor compositional variability. Modest amount of ferric iron ($Fe^{3+}/Fe^{total} = 0.1$) was reasonable for phase-equilibrium modelling, so we ran each RCLC calculation twice: (1) considering ferric iron in each mineral as estimated by the program AX62 (written by T. J. B. Holland and downloaded from his website https://filedn.com/lU1GlyFhv3UuXg5E9dbnWFF/TJBHpages/ax.html on 26 February 2021) and (2) without considering ferric iron.

We also conducted the RCLC thermobarometry using the four different models for Al site occupancy in orthopyroxene described by Pattison et al. (2003).

1. Al on the M site calculated by deficit of Si on the T site $[Al_M = Al_{total} - (2 - Si)]$,
2. Al divided evenly between T and M1 site $[Al_M = Al_{total}/2]$,
3. Al on the M site calculated as a proportion of other elements that might occupy that site $[Al_M = Al_{total}/2/(Fe^{2+} + Mg + Ca + Mn + Al_{total}/2)]$, and
4. Al on the M site calculated as in 2, but with the addition of other elements $[Al_M = (Al_{total} - Fe^{3+} - Cr - 2\cdot Ti)/2]$.

Finally, we considered calculations both with and without biotite and cordierite, in recognition that these minerals appear to have grown during retrogression.

In total, we performed 2000 RCLC calculations—each combination of the five input garnet, orthopyroxene, and plagioclase analyses, repeated with and without ferric iron, with and without cordierite and biotite, and for each Al-in-orthopyroxene site model—to evaluate the sensitivity of the resulting P–T estimates to a range of reasonable input parameters. To facilitate batch processing of the RCLC method, we wrote a script in python that is available with documentation as Appendices S1 and S2 and online at https://github.com/rmholdergeo/batchRCLC (managed by R. M. Holder). The input mineral compositions for RCLC thermobarometry are presented in Tables S1, S8, and S9.

4.4 | Laser ablation split-stream ICP-MS

We measured accessory mineral U–Pb dates and trace element concentrations by laser ablation split-stream (LASS) at UCSB (e.g., Kylander-Clark, 2017; Kylander-Clark et al., 2013). The parameters and standards used for each mineral are listed in Table S13. Trace elements were measured on an Agilent 7700 ICP-MS whereas U, Th, and Pb isotopes were simultaneously measured on a Nu Plasma HR ICP-MS. We measured the lanthanides and Y in zircon and monazite. Hf and Ti were measured in zircon, as well as Zr in rutile. U/Th–Pb dates and trace element contents were calculated using the commercially available software Iolite (Paton, Hellstrom, Paul, Woodhead, & Hergt, 2011; Paton et al., 2010) to correct for down-hole fractionation, mass bias, and machine drift. For each analysis, we report 2-s analytical uncertainties, which include the counting statistics and the reproducibility of the secondary standards during each analytical session (Horstwood et al., 2003). Absolute uncertainties for LASS U–Pb dates are ∼2% based on intralaboratory and interlaboratory reproducibility of reference materials (e.g., Košler et al., 2013; Kylander-Clark et al., 2013), but we report the analytical

uncertainties here because this study focuses on the relative timing of tectonometamorphic events within a single thin section. All LASS data are presented in Tables S5–S7.

5 | RESULTS

5.1 | Al-in-orthopyroxene thermobarometry

RCLC results (Figure S4d and Tables S10–S12) calculated with and without biotite and cordierite differ by only ∼5°C and 0.07 kbar (Table S12); texturally, these minerals appear to be retrograde, so hereafter, we only discuss results calculated without biotite and cordierite. The results without ferric iron ranged 950–1025°C and 8.33–9.45 kbar (Figure S4d). Site Model 1 for Al in orthopyroxene gave the lowest temperatures, and Site Model 2 gave the highest temperatures. The results from calculations in which ferric iron was estimated by stoichiometry ranged 929–1027°C and 8.70–10.12 kbar. The differences between the calculations with and without ferric iron were dependent on the site model used for Al in orthopyroxene. Site Models 2 and 3 resulted in 0.3–0.8 kbar higher pressure when ferric iron was estimated, but differences in temperature were <10°C. Site Model 1 resulted in 0.2–0.5 kbar higher pressure and 8–28°C lower temperature. Site Model 4 resulted in 0.02–0.21 kbar higher pressure and 26–71°C lower temperature.

Pattison et al. (2003) addressed the question of whether to consider Fe^{3+} estimated by stoichiometry in the RCLC calculations. They argued that estimates of very small amounts of ferric iron from stoichiometry (0.02–0.05 atoms per six oxygen for our input orthopyroxene compositions) are imprecise due to the comparable size of the combined uncertainties of the major element measurements (Si, Mg, Fe, and Al). Low estimates of Fe^{3+} are also very sensitive to the accurate and precise measurement of minor and trace elements (Na, Ca, Mn, Cr, and Ti) if those elements are included in the stoichiometric constraints. Pattison et al. (2003) additionally noted that experimental orthopyroxene, from which the thermodynamic data for Al in orthopyroxene were derived, probably had small but unmeasured amounts of ferric iron. Based on this rational and the very small quantities of ferric iron calculated by stoichiometry in our minerals, we suggest the ferric iron-free calculations are the most reliable, although none of the observed variability would significantly change our geological interpretations.

In summary, RCLC Al-in-orthopyroxene thermobarometry for a variety of plausible input parameters indicates that UHTM occurred at ≥930°C and ~9 kbar. Our preferred results are those calculated without estimating ferric iron and which had ranges of 950–1025°C and 8.33–9.45 kbar, depending on the Al-in-orthopyroxene site model used. These pressures and temperatures align with the interpreted peak-temperature mineral assemblage, as well as Al-in-orthopyroxene isopleths calculated for the equilibrium-assemblage diagram of this sample. They also agree with independent P–T estimates conducted on a similar, nearby sample (M89) by Jöns and Schenk (2011).

5.2 | '4^{+}' cation thermometry

Zr-in-rutile transects (454 spot analyses on 10 grains) reveal compositional zoning (Figure 3a). Core Zr concentrations vary among rutile grains from approximately 1200 to 4700 ppm, corresponding to temperatures of ~760°C to ~920°C (P = 8 kbar: Ferry & Watson, 2007). Rutile grains with relatively flat concentration profiles ('R1': rt4, rt5, rt6, and rt9) record the highest temperatures (860–920°C) and are not in contact with ilmenite. Some of these (rt4 and rt9) have diffusive zonation within the outermost 20 µm of their rims (see Section 5.4). Rutile grains with more pronounced concave-down diffusion profiles ('R2': rt1, rt2, rt3, rt8, and rt10) are intergrown with ilmenite and are spatially associated with symplectites around garnet. These yielded lower core temperatures of 760–810°C. One apparently hybrid rutile attached to ilmenite (rt7) records 870°C in its core and has slightly lower Zr content toward the ilmenite. The crystallization of zircon at the expense of rutile (Figure 4d) suggests that rutile expelled Zr as it cooled and it is likely that some or all of the rutile grains do not record peak temperatures.
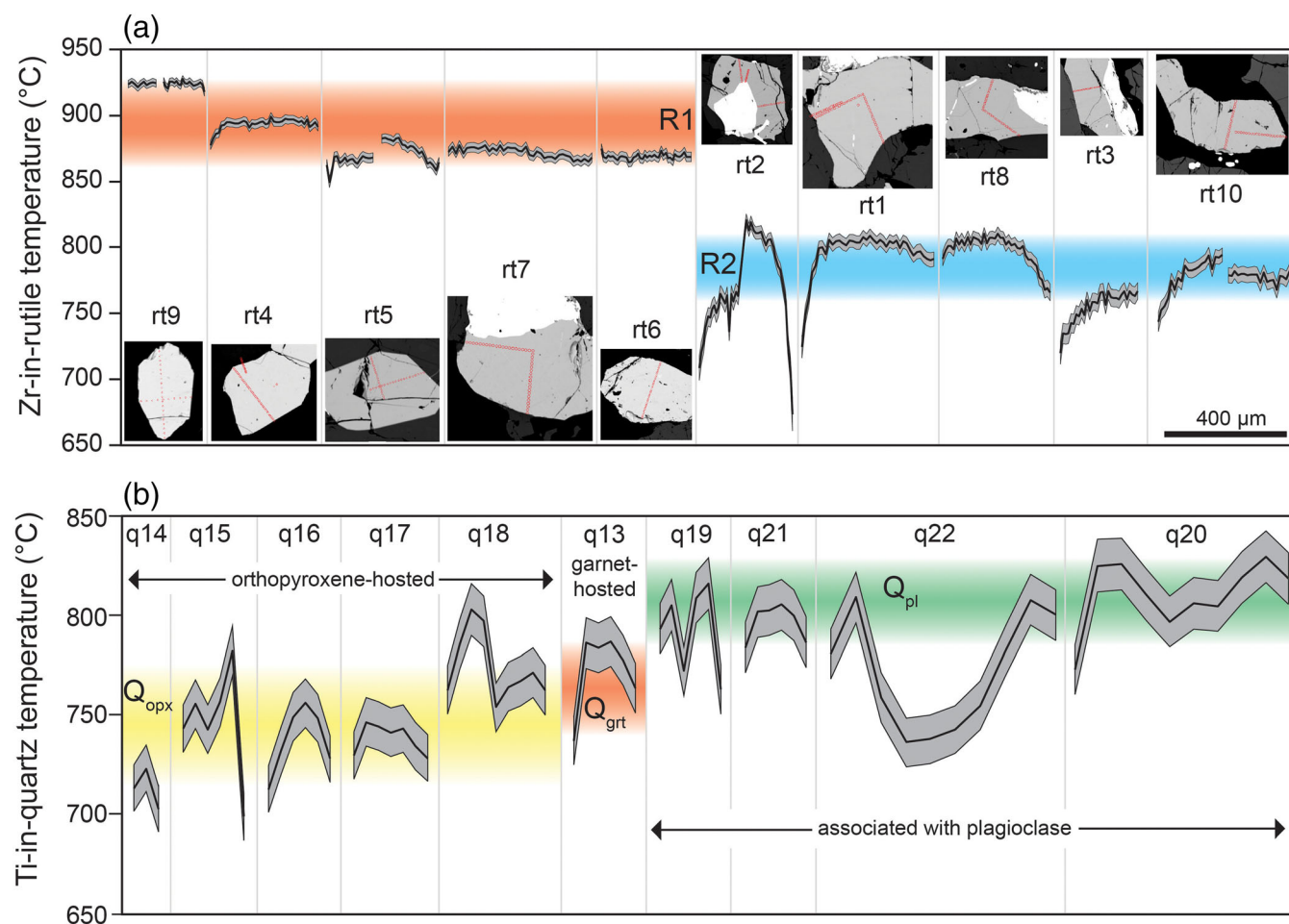
FIGURE 3 4^{+} thermometry results. (a) Zr-in-rutile transects across and backscattered- electron images of the analysed rutile grains. The white mineral associated with many rutile grains is ilmenite. Thin red lines show transect locations, and the results are scaled to match the length of each transect. Grey regions represent 2-s analytical uncertainties at a pressure of 8 kbar. (b) Ti-in-quartz temperature. The grey regions are the calculated temperature at 7.0 ± 0.5 kbar; analytical uncertainties are smaller

Ti concentrations in zircon range from 8 ± 3 to 17 ± 2 ppm and do not vary systematically with date or mineral host. These results correspond to temperatures from $725 \pm 30°C$ to $799 \pm 22°C$ using the Ferry and Watson (2007) Ti-in-zircon calibration and assuming Si and Ti activities of unity. The average temperature is $772 \pm 30°C$ (2 SD). The apparent Ti-in-zircon temperatures are substantially lower than other methods of thermometry, consistent with observations from other recent studies of granulites (Clark et al., 2019; Gervais & Crowley, 2017; Holder, Hacker, et al., 2018). This might be due to decoupling (disequilibrium) of zircon U–Pb dates and trace-element concentrations during granulite-facies metamorphism (Kunz, Regis, & Engi, 2018; Štípská, Powell, Hacker, Holder, & Kylander-Clark, 2016); these temperatures are therefore not interpreted further.

Our Ti-in-quartz results were previously published in Horton et al. (2016), but we re-evaluate them here with respect to their petrologic context and the new thermobarometry. Ti contents in quartz range from 112 to 327 ppm and correspond to minimum Ti-in-quartz temperatures of $699°C$ to $829°C$ (Thomas et al., 2010; Thomas et al., 2015) assuming a pressure of 7 kbar (at 8-kbar temperatures are $\sim20°C$ higher). Within most grains, Ti contents vary by >100 ppm, and the largest (>4 mm) grains (q20 and q22) have concave-up concentration profiles (Figure 3b). Notably, most quartz grains surrounded by orthopyroxene (q14–q17) have lower temperatures ('Q_{opx}': mean of $748°C$ and maximum of $803°C$) compared with those in contact with plagioclase ('Q_{pl}': q19–q22, mean of $788°C$ and max of $826°C$). One apparently orthopyroxene-hosted grain (q18) records temperatures up to $800°C$; we speculate that this grain was near enough to plagioclase (or perhaps exposed to the matrix off the thin section plane) to record temperatures similar to the matrix grains associated with plagioclase (Q_{pl} temperatures). A single garnet-hosted quartz (q13) records an intermediate average temperature of $772°C$ ('Q_{grt}').

5.3 | Phase diagrams

Our interpreted peak phase assemblage of garnet–orthopyroxene–plagioclase–quartz–ilmenite–rutile–melt is stable above 7 kbar and $900°C$ (Figure 5), which agrees with Al-in-orthopyroxene isopleths and the RCLC thermobarometry. The interpreted solidus assemblage, garnet–orthopyroxene–plagioclase–quartz–cordierite–biotite–ilmenite–rutile–melt, is stable in a narrow $P–T$ window at 7.0–7.6 kbar and 750–840°C. The prograde $P–T$ path is inferred to have passed through a field in which cordierite and garnet were both stable, based on the cordierite inclusion in garnet; using the melt-reintegrated phase diagram (Figure 5b), this is ~7 kbar. The modes of minerals observed in thin section (Table 1) match well with the calculated volume percent of each mineral in the phase diagram for the interpreted solidus paragenesis (Figures S2 and S3).

5.4 | Petrochronology

The U–Pb zircon results presented here supplement those in Horton et al. (2016). Several discordant analyses from detrital cores fall on a mixing line that intersects concordia at *c.* 2200 Ma, consistent with their derivation from the adjacent Androyen domain or an older basement beneath the Anosyen domain (Tucker et al., 2014). Analyses that partially sampled inherited cores (Figure 4c) are enriched in heavy rare earth elements (HREEs) relative to analyses that only sampled metamorphic growth rims. The young concordant dates for mixed rim and core analyses suggests that the U–Pb and REE systems are decoupled due to Pb—but not HREE—loss from the cores during metamorphism (e.g., Štípská et al., 2016). The low HREE analyses are therefore the most reliable for recording metamorphism. Concordant dates with low HREE associated with Pan-African orogenesis span roughly 100 Ma from 617 ± 9 to 516 ± 7 Ma. Based on the zircon date distribution, the main stage of zircon growth began at *c.* 560 Ma and culminated at *c.* 530 Ma. Some zircons appear to have grown at the expense of rutile during and after this main stage of zircon growth (Figure 4d). Some metamorphic zircon dates are as young as 516 ± 7 Ma. The low HREE content of the metamorphic zircon is consistent with garnet having been stable over the entire period recorded by these dates (Foster et al., 2000; Rubatto, 2002).

Nearly all monazite U–Pb dates ($n = 180$) form a single population (Figure 4e) with a weighted mean of 537 Ma (2 SD, ± 8 Ma; assuming 2% accuracy, ±11 Ma); we interpret the oscillatory and sector zoning visible in EMPA Y and Th maps to indicate that growth occurred in the presence of melt (Figure 4e,f). Based on the high temperature of metamorphism and unimodal date distribution, this date likely records monazite (re)crystallization as the rock cooled from peak temperature to the solidus (e.g., Stepanov et al., 2012; Yakymchuk, 2017). This interpretation is consistent with the observation that monazite occurs primarily with cordierite and biotite, minerals that also likely formed as the rock decompressed and cooled to the solidus. Embayments along monazite edges cut across the sector zoning, indicating
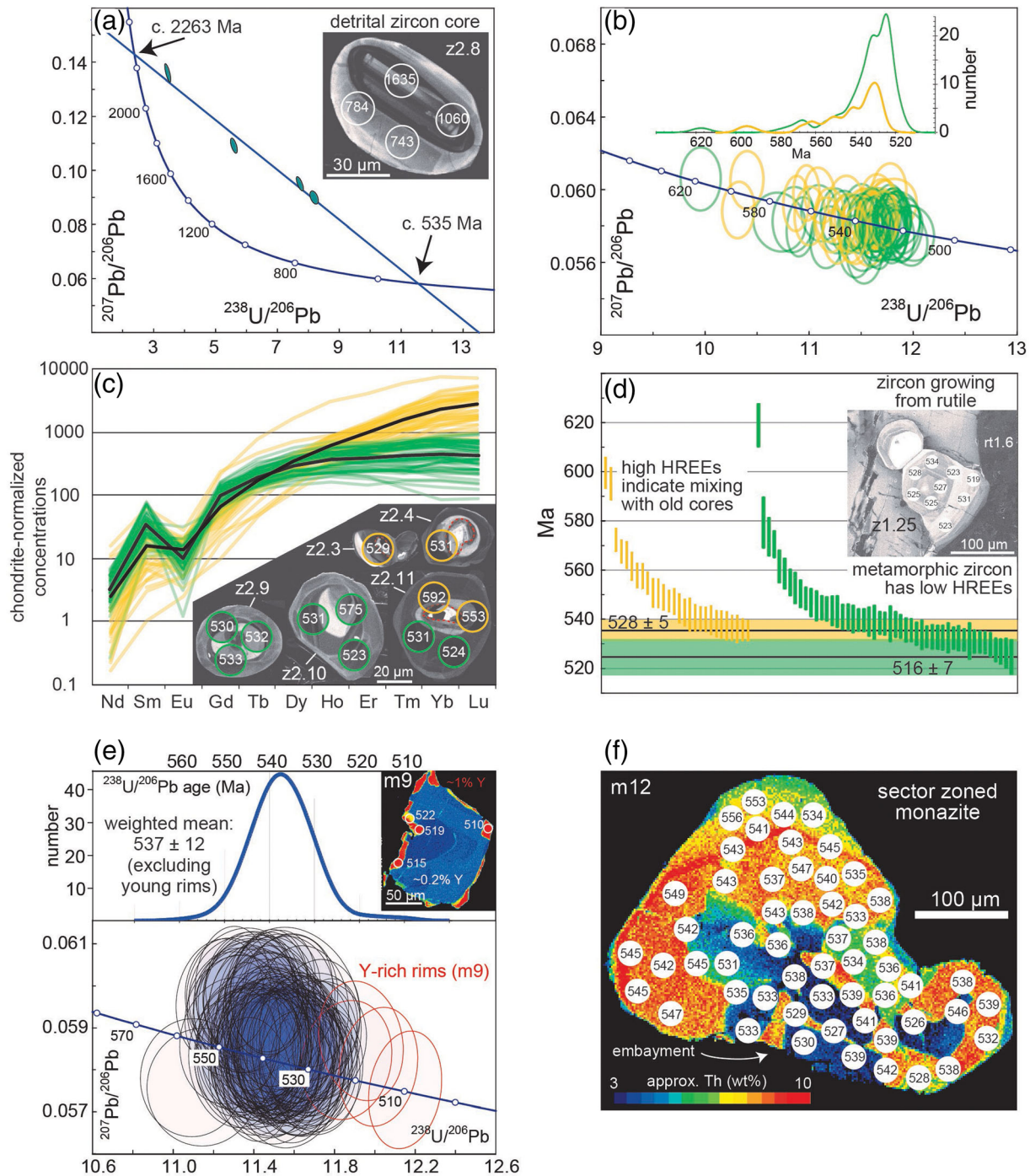
FIGURE 4 Zircon and monazite petrochronology. (a) Spot analyses on this zircon yielded discordant ages that indicate mixing between a Palaeoproterozoic core and a Neoproterozoic rim. (b) Concordant metamorphic zircon rim analyses indicate that the main stage of metamorphism may have begun by 610 Ma and definitely began by 560–580 Ma. Yellow analyses have high heavy rare earth elements (HREEs), and green analyses have low HREEs. (c) Elevated HREE abundance is attributable to mixing between HREE-rich cores (outlined with a dashed red line in zircons Z2.4 and Z2.11) and HREE-poor rims with variable CL brightness. (d) Analyses with depleted HREEs (green) extend to younger dates. The inset shows zircon grown from a rutile during retrograde metamorphism c. 530–520 Ma. (e) Sector-zoned monazites, spatially associated with cordierite and biotite, yielded a single population of dates c. 537 Ma, whereas Y-rich rims are younger. The concordia diagram shows all monazite analyses in this study. The inset shows an electron microprobe analysis (EMPA) Y map of monazite m9. (f) EMPA Th map of monazite m12 shows sector zoning cut by embayments but indistinguishable dates among different compositional domains. Dates for each analysis are listed in Ma and have ~8 Ma 2-s analytical precision. Error ellipses and bars represent 2-s uncertainties
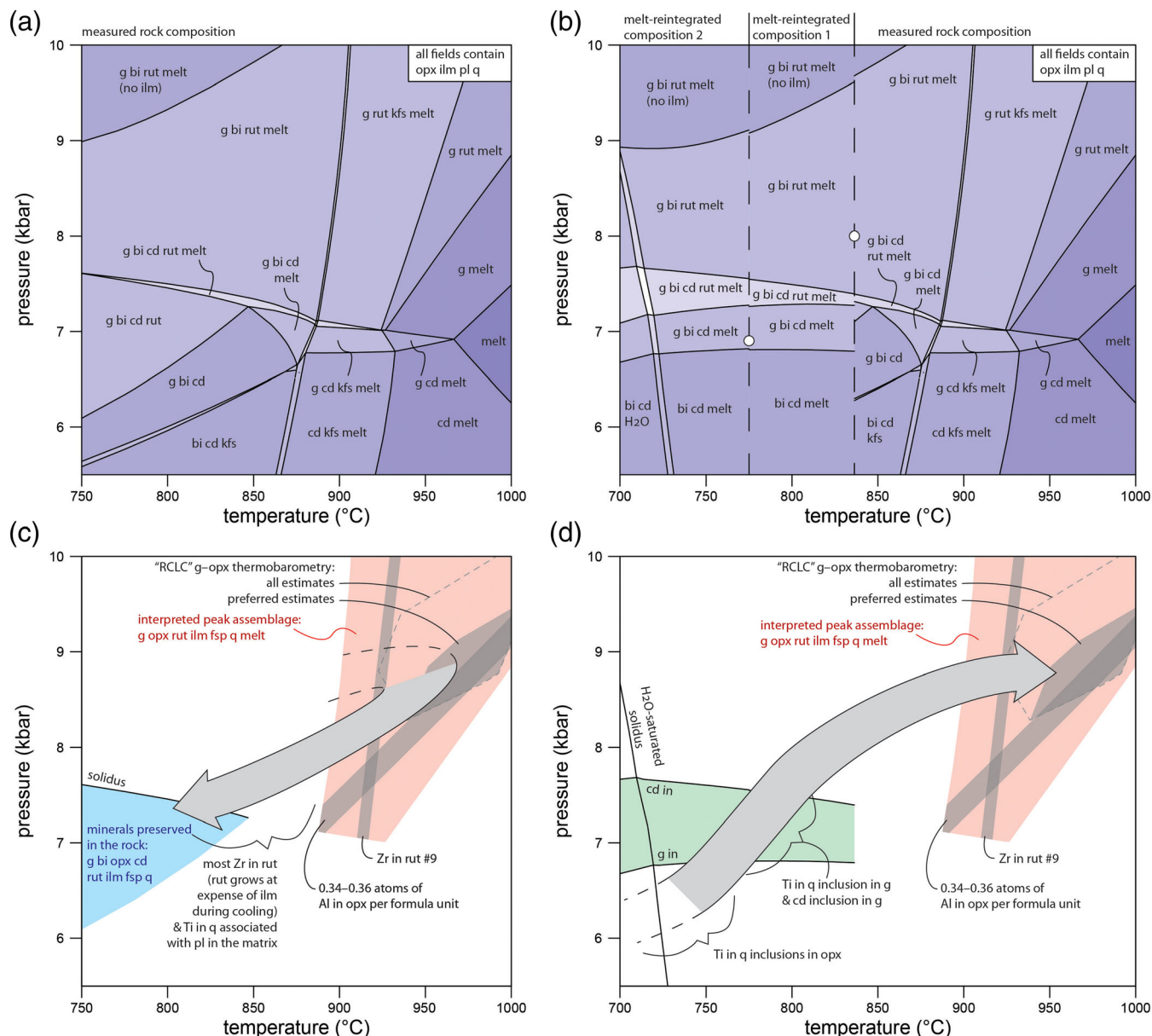
FIGURE 5 (a) Retrograde and (b) prograde phase diagrams showing equilibrium mineral assemblages. The right-hand side of panel (b) and all of panel (a) were calculated using the estimated rock composition. The left-hand portion of panel (b) is based on the inferred melt-reintegrated compositions of the rock. For mineral modes, see Figure S3. Panels (c) and (d) show the inferred *P–T–t* path (grey arrows) during retrograde and prograde metamorphism, respectively. Grey shaded regions represent thermobarometric constraints (see text for details). Green, red, and blue regions correspond to key prograde, peak, and retrograde mineral assemblages, respectively

that monazite resorption or recrystallization occurred after the main stage of growth. Several analyses targeting thin (5–10 μm) Y-rich rims that overgrew these embayments yielded younger dates (down to 510 ± 6) and have slightly elevated HREEs compared with the core analyses (Figure 4e). This is consistent with formation during or after garnet breakdown to form the cordierite–orthopyroxene symplectites below the solidus.

Concordant rutile U–Pb dates are all less than 500 Ma (Figure 6b), with the exception of a single concordant date of 540 ± 14 Ma. The youngest rutile date is 461 ± 10 Ma and dates obtained from one grain (rt6) extend to 493 ± 11 Ma. Pb diffusion through rutile is considerably faster than through monazite and zircon, so these rutile U–Pb dates probably indicate closure below ~600°C (Cherniak, 2000) or subsequent resetting.

5.5 | Diffusion chronometry

Although the interiors of high-Zr rutiles are relatively homogenous, some grains exhibit diffusive zoning toward their rims. Our EMPA rim profile of rt4 with 3-μm spacing (Figure 6a) shows that Zr and Nb decrease toward the edge of the grain. To evaluate this zoning, we used an alternating direction, implicit, finite-difference model modified from Hinojosa and Mickus (2002) with a cylindrical geometry. For Nb, we used a pre-exponential factor of 5.3×10^{-3} m^2/s and an activation energy of 377.5 kJ/mol (Marschall et al., 2013). For Zr, we used a pre-exponential factor of 9.8×10^{-15} m^2/s and an activation energy of 170 kJ/mol (Cherniak et al., 2007). The modelled rutile has a radius of 100 μm and height of 500 μm, with 5-μm nodes. Assuming initial uniform concentrations of Nb (1500 ppm) and Zr (3600 ppm) and boundary conditions of zero, we optimized the temperature and duration of the model to produce a radial diffusion profiles similar to the rt4 results. We were able to closely approximate rt4 diffusion profiles by running the model at 600°C for 0.5 Ma (Figure 6a); although this is not a unique solution, it is clear that the diffusion occurred at subgranulite facies conditions and was short lived. Use of more recent diffusion data (Dohmen et al., 2019) does not significantly change this result.
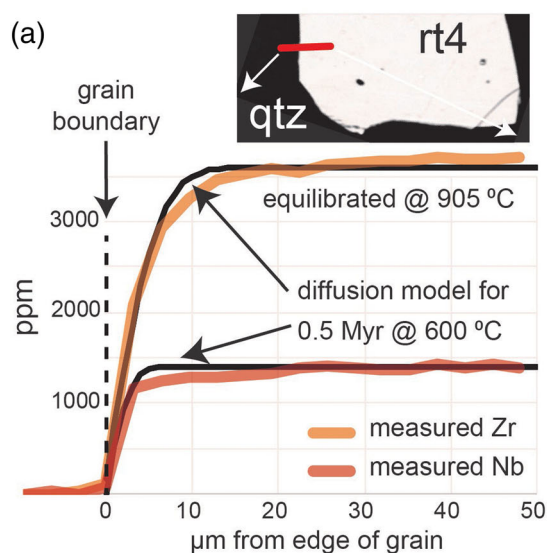
6 | DISCUSSION

6.1 | Reconstructing the *P–T–t* path

Collectively, our results imply a clockwise *P–T* path, which is consistent with some previously proposed (Figure S1) for Madagascar (Jöns & Schenk, 2011) and reaches higher *P* than inferred by other studies (e.g., Boger et al., 2012; Holder, Hacker, et al., 2018). For clarity, we chronologically organize these new constraints into five stages along our inferred *P–T–t* path.

6.1.1 | Stage 1: Heating to >725°C at <7.5 kbar

We conclude that orthopyroxene-hosted quartz (Q_{opx}) grains equilibrated along the prograde path before becoming surrounded orthopyroxene (Figure S3f). Hereafter, we refer to this first stage of orthopyroxene growth as 'opx1', the next generation of orthopyroxene as 'opx2', and so on (we use the abbreviation crd- for cordierite growth stages in the same manner). Evidence that orthopyroxene shielded quartz grains (Q_{opx}) from subsequent resetting includes their relatively flat Ti concentration profiles and the observation that plagioclase-associated quartz grains (Q_{pl})—unshielded
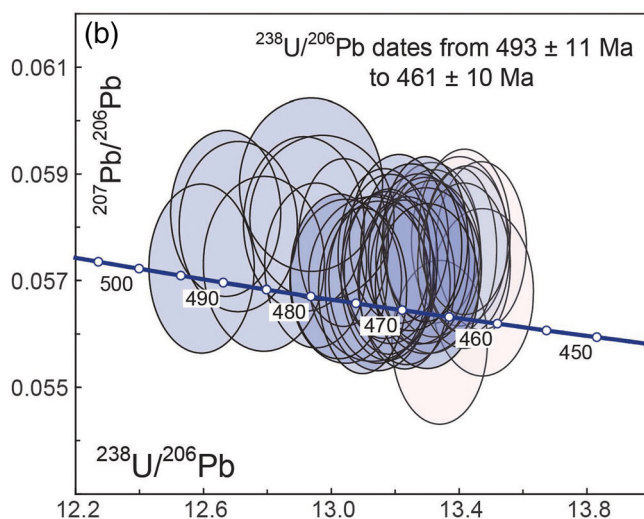
FIGURE 6 (a) Diffusive loss of Zr and Nb from rutile rims constrains the temperature and duration of the diffusive event. A finite-difference model run for 0.5 Ma at 600°C approximates the diffusive zonation. Such a short duration and low temperature suggests that metasomatism triggered a brief stage of retrogression during cooling. (b) U–Pb zircon dates suggest that rutile cooled through a Pb-closure temperature of ~600°C by 460 Ma, which may approximate the age of the metasomatic event

and more susceptible to resetting—exhibit Ti profiles indicative of incomplete equilibration at higher temperatures. Ti-in-quartz thermometry implies that Q_{opx} were trapped at $\sim725°C$. This entrapment temperature, as well as the presence of prograde cordierite (crd1) included in garnet, is consistent with modelled peritectic orthopyroxene growth at <7.5 kbar during the earliest stage of partial melting.

6.1.2 | Stage 2: Burial to ~9 kbar

Garnet began growing at ~6.5 kbar during burial at the expense of orthopyroxene and cordierite (Figure S3d). Garnet-hosted quartz (Q_{grt}) records an average temperature of 760°C, 35°C higher than Stage 1 quartz, indicating heating before and/or during garnet growth. The inclusion of cordierite in garnet, and absence of cordierite outside of retrograde textures in the matrix, implies an increase in pressure to >7 kbar. Our calculated peak pressure of ~9 kbar is at the lower end of the 8- to 11-kbar estimate of Jöns and Schenk (2011) for samples for the same location and Martelat et al. (2012) for samples in a shear zone near Ihosy, comparable with estimates of peak pressure by Martelat et al. (1997) and Markl et al. (2000) in the Androyen domain to the west, and 2 kbar higher than the peak pressure estimate of Boger et al. (2012) in the Anosyen domain, to the east. Because these studies investigated samples collected across a broad area and used different thermobarometry methods based on different thermodynamic data, we consider the differences in pressure reported in these studies to be relatively minor. The slightly lower pressure estimates for the Anosyen domain to the east are largely based on the absence of garnet in many Ihosy Formation samples (oxidized metapelites and cordierite–sillimanite gneisses) across the Anosyen domain. However, where garnet is present in the Ihosy Formation, it is rimmed by cordierite and orthopyroxene (GAF-BGR, 2008), suggesting that retrograde reactions consumed garnet except in the most aluminous rocks that grew larger garnets, such as F2910B. It remains uncertain whether the lack of garnet elsewhere in the Ihosy Formation (a) indicates that the sample of this study exhumed from greater depths within the Beraketa shear zone than rocks in the Anosyen domain to the east or (b) is due to pervasive retrogression across the Anosyen domain.

6.1.3 | Stage 3: Heating past 960°C

RCLC thermobarometry and Al-in-orthopyroxene isopleths are consistent with peak metamorphism at 950–

1000°C and ~9 kbar. Reaching these conditions from Stage 2 implies heating at >100°C/kbar and orthopyroxene growth (opx2) at the expense of garnet (Figures S3d and S3f). This stage of metamorphism is poorly recorded by rutile and quartz, probably because both minerals would have been consumed along such a path (Figure S3j): rutile would have partially broken down to ilmenite, and quartz would have been consumed by partial melting (Figure S3l). Furthermore, any grains not shielded as inclusions probably diffusively re-equilibrated.

6.1.4 | Stage 4: Cooling and decompression to the solidus

Some of the rutile preserved in the rock likely grew during Stage 2 burial and briefly during Stage 3 heating past the biotite-out reaction at $\sim890°C$. However, as mentioned above, the flat compositional profiles in R1 may be indicative of complete Zr-in-rutile equilibration at suprasolidus conditions. The recorded temperatures in R1 could record the Stage 3 heating (for inclusions in orthopyroxene, opx2) and/or Stage 4 cooling (for inclusions in plagioclase and associated with cordierite in the matrix). In either case, isolation from the rest of the rock would have facilitated preservation of the high Zr concentrations. The absence of R1 Zr-in-rutile temperatures corresponding to the peak temperature determined from the phase diagram and Al in orthopyroxene (except for a single grain: rt9) is consistent with modelled rutile abundances (Figures S3k and S3l); the mode of rutile is predicted to have decreased approaching peak temperature (to form ilmenite) and increased again as the rock cooled (at the expense of ilmenite). Cooling along this path would have also caused garnet growth at the expense of opx1 and opx2 (Figure S3c), a reversal of the prograde reaction among these minerals during Stage 3.

We infer that the presence of melt and high temperatures in the system efficiently promoted mineral-melt reactions in the direction of the equilibrium assemblage above the solidus. When the rock passed through the solidus during retrogression, reactions may have ceased except where local fluids or subsolidus symplectites formed, as is generally assumed for the preservation of granulite facies mineral assemblages (e.g., Spear et al., 1999; White & Powell, 2002). The inferred solidus assemblage intersects the solidus at ≤840°C, which corresponds to the Ti contents in the rims of quartz in the matrix associated with plagioclase (Q_{pl}). These Ti concentrations may reflect arrested inward Ti diffusion or quartz growth near the solidus. R2 cores also record

temperatures of ~800°C that likely reflect arrested Zr re-equilibration with the matrix as melt crystallized and grain-boundary diffusion became ineffective (e.g., Kohn et al., 2016).

6.1.5 | Stage 5: Subsolidus reactions

Symplectites grew by the apparent reaction: garnet → orthopyroxene (opx3) + cordierite (crd3). Ilmenite grew at the expense of rutile where Fe was available, which explains why rutile-ilmenite inter-growths are most abundant near opx3–crd3 symplectites. Rutiles in these areas have concave-down Zr concentrations (R2) and record the loss of Zr at <800°C (assuming SiO_2 and $ZrSiO_4$ activities of unity) during these sub-solidus reactions. Rutiles away from symplectites (R1) appear unaffected by these reactions; the thin diffusive zonation along their rims might have occurred later, at ~600°C, based on our diffusion chronometry results.

6.2 | Chronologic constraints

6.2.1 | 580–560 to 540 Ma: Burial and heating

A histogram of zircon U–Pb dates shows an increase in the frequency of dates at 580–560 Ma (Figure 4b). Older concordant analyses (620–600 Ma) represent either an earlier onset to metamorphism, consistent with widespread similar dates in the Androyen domain to the west (e.g., Tucker et al., 2014) and much more rarely in the Anosyen domain to the east (Horton et al., 2016; Jöns & Schenk, 2011), or are mixing with a detrital igneous component (such as 2200 Ma). A conservative interpretation is that Pan-African metamorphic zircon had begun (re)crystallizing by 580–560 Ma. The depleted HREEs for these zircons indicate that they grew in the presence of garnet and therefore during and after Stage 2 burial; temperatures were therefore >700°C by 560 Ma.

6.2.2 | 540–530 Ma: Retrogression from peak metamorphism to the solidus

The culmination of zircon and monazite growth occurred at 540–530 Ma, which we interpret as the interval of cooling from peak conditions to the solidus. The monazite data are particularly homogeneous, constraining the timing of high-temperature cooling and melt crystallization to 537 ± 11 Ma. If this interpretation is correct, peak metamorphism occurred at or immediately before this time. The fact that biotite has a weak preferred alignment (Figure 2a) suggests that the Beraketa shear zone was active during the early stages of cooling, around the time the rock passed through the solidus. These monazites and zircons have depleted HREEs, consistent with the observed survival of garnet during high-temperature retrogression. Rutile (e.g., Grain 6: Horton et al., 2016) on which zircon grew (Figure 4d: 535–519 Ma) records temperatures of 830–850°C; this particular zircon growth probably occurred near or below the solidus.

6.2.3 | 530–510 Ma: Minor retrogression and symplectite growth

Zircon associated with symplectites and grown on rutile has dates down to 516 ± 7 Ma, whereas Y-rich rims on monazites have dates as young as 510 ± 6 Ma. We associate these dates with (a) minor subsolidus metasomatism that resulted in Zr exsolution from rutile to form new zircon and (b) symplectite formation and liberation of HREE from garnet that allowed for the formation of Y + HREE rims on monazite, respectively.

6.2.4 | 490–460 Ma: Retrograde metasomatism

With the exception of one outlier, rutile dates range from 493 ± 11 to 461 ± 10 Ma. The lower end of this range is distinctly younger than K–Ar (491–485 Ma), $^{40}Ar/^{39}Ar$ (481 ± 2 Ma), and Rb–Sr (491 ± 10 Ma) phlogopite dates from elsewhere in southern Madagascar (Martin et al., 2014; references therein) and is equivalent to c. 455 Ma $^{40}Ar/^{39}Ar$ dates from Itrongay pegmatite feldspar in the Androyen domain to the northwest (Popov et al., 2020). This is surprising because Pb diffuses more slowly in rutile than Ar does in phlogopite or feldspar, so closure of Pb in rutile is expected at higher temperatures (~600°C) than Ar in phlogopite and feldspar (<500°C, depending on grain size). Excess Ar is observed in many biotites, perhaps because Ar is more soluble in biotite than the surrounding minerals (Kelley & Wartho, 2000). If so, the younger U–Pb ages in rutile may provide a better regional cooling age. On the other hand, U–Pb rutile dates are not uniform as would be predicted for Pb closure in similarly sized grains, so metasomatic resetting seems probable. Rutile diffusion chronometry is consistent with a short-lived—less than 0.5 Ma—local fluid-related event having occurred near the Pb-closure temperature, so we infer that fluids partially reset U–Pb ages at ~460 Ma. It follows that the rock must have

cooled below 600°C by that time to preserve the heterogeneity of dates observed.

6.3 | Heating rates and mechanisms

Some combination of mechanical heating, radiogenic heating, conduction, and injection of mantle-derived magmas into the crust may explain the UHTM conditions recorded in Beraketa shear zone and elsewhere in southern Madagascar. We can rule out mechanical heating (also referred to as shear heating) as the primary source of heat for heating beyond amphibolite facies because the negative feedback between heating and thermal weakening severely limits mechanical heat production above 600°C (Stüwe, 1998). Below, we explore the possible role of the other heating mechanisms.

The $P–T–t$ history of sample FH2910B constrains the rates of prograde processes. Heating and burial from the garnet-in reaction to peak conditions (Stages 2 and 3) occurred at time-averaged rates of 7–14°C/Ma and 0.2–0.4 km/Ma, assuming an increase from 700 to 970°C and from 6.5 to 9.0 kbar between 580 and 560 and 540 Ma. These rates are in agreement with the $T–t$ path estimated by Holder, Hacker, et al. (2018), for which the heating rate was 10–17°C/Ma. These rates are inconsistent with focused radiogenic heat production as the sole source of heat for UHTM, although they do not rule it out as an important component. Static thermal models based on the natural, high distribution of heat-producing elements across southern Madagascar led to high-temperature heating rates of ≤3°C/Ma for the granulite facies, and could not reproduce temperatures greater than 950°C at depths ≤30 km in less than 40 Ma (Horton et al., 2016) unless the mantle heat flow is greater than 30 mW/m^2. If burial and heating were continuous from c. 620 Ma (as possibly suggested by 620–600 Ma dates in the Androyen domain to the west and rare 620–600 Ma dates in the Anosyen to the east; Jöns & Schenk, 2011; Horton et al., 2016; this study), heating to ~900°C could have occurred by 540 Ma in these models with a lower mantle heat flow. However, the scarcity of old metamorphic dates in, and to the east of, the Beraketa shear zone leads us to believe that the main stage of metamorphism relevant to this sample began at c. 580 Ma. If so, our inference of 7–14°C/Ma heating from Stages 2 to 3 is two to five times faster than the ≤3°C/Ma calculated for radiogenic heating alone. Thus, our results suggest that radiogenic heating in southern Madagascar was not the sole cause of UHTM. The need for a component of non-radiogenic heating is also visible in the shape of the $P–T$ path, which is a much narrower clockwise loop with a lower pressure of prograde metamorphism (6–8 kbar;

similar to that of Boger et al., 2012) than predicted by models of conductive heating in collisional orogenesis (e.g., England & Thompson, 1984).

High conductive heat flow from the mantle (Horton et al., 2016), possibly due a thin mantle lithosphere (Holder, Hacker, et al., 2018; Moyen, 2020), can increase the rate of crustal heating substantially. Lithosphere beneath vertical shear zones—possible conduits for fluids and heat—may have thinned due to the rheological contrast between the weak upper mantle and the stronger granulitic lower crust (Martelat et al., 2020). Even if radiogenic heat production is high (Horton et al., 2016), conductive heating of a thickened orogenic crust to >900°C in <40 Ma likely requires elevated mantle heat flow (e.g., from mantle lithosphere thicknesses <80 km; Holder, Hacker, et al., 2018). Such a thin mantle lithosphere exists beneath central Tibet today (Tunini et al., 2016) but whether southern Madagascar was similar is speculative. In contrast, Boger et al. (2012) proposed that the Anosyen domain represents an inverted backarc basin or continental margin that was neither significantly thickened nor exhumed during metamorphism. This could be broadly consistent with the narrow $P–T$ paths in this study and Boger et al. (2012) but is at odds with other studies that propose larger changes in pressure (e.g., Jöns & Schenk, 2011; Martelat et al., 2012).

Hypothesized mantle heat advection in the form of mantle magma injection into the crust (Holder, Hacker, et al., 2018; Jöns & Schenk, 2011) remains untested. Plutons emplaced during orogenesis—referred to as the Ambalavao Suite—range in age from 570 to 520 Ma (GAF-BGR, 2008). The suite exhibits two geochemical trends: (1) gabbro and geochemically associated quartz monzonite and (2) peraluminous granites that commonly contain garnet, spinel, and/or orthopyroxene that attest to their high crystallization temperatures. The suite might therefore be a mixture of mantle-derived magma (gabbro and monzonite) and partial melts of surrounding metasedimentary crust (peraluminous granites). The Ambalavao plutons are notably more voluminous in the southeastern Anosyen domain, where they form a batholith, than in the Beraketa shear zone, even though peak temperatures are not detectably different in these areas. Future work on the age and origins of the Ambalavao Suite might establish causal links between magmatism and UHTM. For now, it remains speculative.

6.4 | Retrograde rates and processes

The sample cooled and exhumed from peak conditions to the solidus (Stage 4) at minimum rates of 14°C/Ma and 0.45 km/Ma, assuming 140°C of cooling and 1.5 kbar of

decompression in ≤10 Ma (limited by the precision and accuracy of the LA-ICP-MS geochronology). This cooling rate is consistent with previous estimates for the Anosyen domain (17 ± 7°C/Ma: Holder, Hacker, et al., 2018; Montel et al., 2018) and implies that exhumation from peak conditions to the solidus and concomitant cooling occurred at rates comparable with heating and burial. Stage 5 cooling from the solidus through Pb closure in rutile (a decrease of 260°C over 66 Ma) may have slowed to ~4°C/Ma. This last estimate should be viewed with caution, however, because our rutile ages are difficult to reconcile with other thermochronology from southern Madagascar (Martin et al., 2014; Montel et al., 2018; Popov et al., 2020). The origins and composition of the fluids responsible for possible metasomatic Pb loss from rutile are unknown. Residual hydrous fluids likely persisted in the Beraketa shear zone after the crust cooled through the solidus (Martelat et al., 2014). The Beraketa shear zone may have also been infiltrated by CO_2- and H_2O-rich fluids derived from the mantle (Martin et al., 2014; Pili et al., 1997). Regardless, regional cooling likely decelerated as the sample passed through the solidus.

Our interpretation that heating beyond biotite breakdown on the prograde path produced ≥12 vol.% partial melt raises the possibility that the crust was significantly weakened by melting (e.g., Rosenberg & Handy, 2005) around 540 Ma. That the retrograde metamorphism was nearly isobaric suggests that the overlying crust did not undergo catastrophic thinning. The granulites of southern Madagascar may have exhumed, in part, by transpression along the terrane-bounding Beraketa and Ampanihy shear zones (e.g., Martelat et al., 2000). One explanation for a pronounced decrease in cooling rate is that the disappearance of melt added enough rigidity within the Beraketa shear zone to limit deformation and thereby arrest vertical exhumation (Rosenberg & Handy, 2005). If so, partially exhumed crust might have remained trapped at ~20-km depth, where it underwent limited cooling. The latent heat of melt crystallization (Stüwe,) throughout the region is also likely to have slowed cooling substantially. These processes help explain why UHTM is not ephemeral in collisional orogens.

AUTHOR CONTRIBUTIONS
F. Horton conceptualized the study, curated the data, conducted the formal analysis, acquired the funding, conducted the investigation, administered the project, supervised the study, and wrote the original draft of the manuscript. R. M. Holder curated the data, conducted the formal analysis, acquired the funding, conducted the investigation, designed the methodology, prepared the software, validated the results, and reviewed and edited the manuscript. C. R. Swindle conducted the formal analysis, validated the results, and reviewed and edited the manuscript.

DATA AVAILABILITY STATEMENT
All data are available upon request. The python code used for the RCLC calculations can be found in Appendices S1 and S2, as well as at https://github.com/rmholdergeo/batchRCLC or by correspondence with R. Holder.

ORCID
Forrest Horton https://orcid.org/0000-0001-9524-8874
Robert M. Holder https://orcid.org/0000-0002-1119-6905

REFERENCES

Bartoli, O. (2017). Phase equilibria modelling of residual migmatites and granulites: An evaluation of the melt-reintegration approach. *Journal of Metamorphic Geology*, *35*(8), 919–942. https://doi.org/10.1111/jmg.12261

Beaumont, C., Jamieson, R. A., Nguyen, M. H., & Medvedev, S. (2004). Crustal channel flows: 1. Numerical models with applications to the tectonics of the Himalayan-Tibetan orogen. *Journal of Geophysical Research: Solid Earth*, *109*(B6), 1–29. https://doi.org/10.1029/2003jb002809

Boger, S. D., Hirdes, W., Ferreira, C. A. M., Jenett, T., Dallwig, R., & Fanning, C. M. (2015). The 580–520 Ma Gondwana suture of Madagascar and its continuation into Antarctica and Africa. *Gondwana Research*, *28*(3), 1048–1060. https://doi.org/10.1016/j.gr.2014.08.017

Boger, S. D., Hirdes, W., Ferreira, C. A. M., Schulte, B., Jenett, T., & Fanning, C. M. (2014). From passive margin to volcano–sedimentary forearc: The Tonian to Cryogenian evolution of the Anosyen Domain of southeastern Madagascar. *Precambrian Research*, *247*, 159–186. https://doi.org/10.1016/j.precamres.2014.04.004

Boger, S. D., Maas, R., Pastuhov, M., Macey, P. H., Hirdes, W., Schulte, B., Fanning, C. M., Ferreira, C. A. M., Jenett, T., & Dallwig, R. (2019). The tectonic domains of southern and western Madagascar. *Precambrian Research*, *327*, 144–175. https://doi.org/10.1016/j.precamres.2019.03.005

Boger, S. D., White, R. W., & Schulte, B. (2012). The importance of iron speciation (Fe^{+2}/Fe^{+3}) in determining mineral assemblages: An example from the high-grade aluminous metapelites of southeastern Madagascar. *Journal of Metamorphic Geology*, 30(9), 997–1018. https://doi.org/10.1111/jmg.12001

Chacko, T. (1996). Ultra-high temperature metamorphism in the Kerala Khondalite Belt. The Archaean and Proterozoic terrains in southern India within east Gondowana. *Gondowana Research Group Memoir*, 3, 157–165.

Cherniak, D. J. (2000). Pb diffusion in rutile. *Contributions to Mineralogy and Petrology*, 139, 198–207. https://doi.org/10.1007/PL00007671

Cherniak, D. J., Manchester, J., & Watson, E. B. (2007). Zr and Hf diffusion in rutile. *Earth and Planetary Science Letters*, 261(1–2), 267–279. https://doi.org/10.1016/j.epsl.2007.06.027

Clark, C., Fitzsimons, I. C. W., Healy, D., & Harley, S. L. (2011). How does the continental crust get really hot? *Elements*, 7(4), 235–240. https://doi.org/10.2113/gselements.7.4.235

Clark, C., Taylor, R. J., Johnson, T. E., Harley, S. L., Fitzsimons, I. C., & Oliver, L. (2019). Testing the fidelity of thermometers at ultrahigh temperatures. *Journal of Metamorphic Geology*, 37(7), 917–934. https://doi.org/10.1111/jmg.12486

Clemens, J. D., & Vielzeuf, D. (1987). Constraints on melting and magma production in the crust. *Earth and Planetary Science Letters*, 86(2–4), 287–306. https://doi.org/10.1016/0012-821X(87)90227-5

Collins, A. S., Kinny, P. D., & Razakamanana, T. (2012). Depositional age, provenance and metamorphic age of metasedimentary rocks from southern Madagascar. *Gondwana Research*, 21(2), 353–361. https://doi.org/10.1016/j.gr.2010.12.006

de Wit, M. J., Bowring, S. A., Ashwal, L. D., Randrianasolo, L. G., Morel, V. P. I., & Rambeloson, R. A. (2001). Age and tectonic evolution of Neoproterozoic ductile shear zones in southwestern Madagascar, with implications for Gondwana studies. *Tectonics*, 20(1), 1–45. https://doi.org/10.1029/2000TC900026

Dohmen, R., Marschall, H. R., Ludwig, T., & Polednia, J. (2019). Diffusion of Zr, Hf, Nb and Ta in rutile: Effects of temperature, oxygen fugacity, and doping level, and relation to rutile point defect chemistry. *Physics and Chemistry of Minerals*, 46(3), 311–332. https://doi.org/10.1007/s00269-018-1005-7

England, P. C., & Thompson, A. B. (1984). Pressure—temperature—time paths of regional metamorphism I. Heat transfer during the evolution of regions of thickened continental crust. *Journal of Petrology*, 25(4), 894–928. https://doi.org/10.1093/petrology/25.4.894

Ferry, J. M., & Watson, E. B. (2007). New thermodynamic models and revised calibrations for the Ti-in-zircon and Zr-in-rutile thermometers. *Contributions to Mineralogy and Petrology*, 154(4), 429–437. https://doi.org/10.1007/s00410-007-0201-0

Fitzsimons, I. C. (2016). Pan–African granulites of Madagascar and southern India: Gondwana assembly and parallels with modern Tibet. *Journal of Mineralogical and Petrological Sciences*, 111(2), 73–88. https://doi.org/10.2465/jmps.151117

Foster, G., Kinny, P., Vance, D., Prince, C., & Harris, N. (2000). The significance of monazite U–Th–Pb age data in metamorphic assemblages; a combined study of monazite and garnet chronometry. *Earth and Planetary Science Letters*, 181, 327–340. https://doi.org/10.1016/S0012-821X(00)00212-0

Fritz, H., Abdelsalam, M., Ali, K. A., Bingen, B., Collins, A. S., Fowler, A. R., Ghebreab, W., Hauzenberger, C. A., Johnson, P. R., & Kusky, T. M. (2013). Orogen styles in the East African Orogen: A review of the Neoproterozoic to Cambrian tectonic evolution. *Journal of African Earth Sciences*, 86, 65–106. https://doi.org/10.1016/j.jafrearsci.2013.06.004

GAF-BGR. (2008). Final report: Réalisation des travaux de cartographie géologique de Madagascar, révision approfondie de la cartographie géologique et minière aux échelles 1/100 000 et 1/500 000 zone Sud. République de Madagascar, Ministère de l'Energie et des Mines EM/SG/DG/UCP/PGRM (162 pp.).

Ganne, J., Nédélec, A., Grégoire, V., Gouy, S., & de Parseval, P. (2014). Tracking Late-Pan-African fluid composition evolution in the ductile crust of Madagascar: Insight from phase relation modelling of retrogressed gneisses (province of Fianarantsoa). *Journal of African Earth Sciences*, 94, 100–110. https://doi.org/10.1016/j.jafrearsci.2013.10.004

Gervais, F., & Crowley, J. L. (2017). Prograde and near-peak zircon growth in a migmatitic pelitic schist of the southeastern Canadian Cordillera. *Lithos*, 282–283, 65–81.

Gerya, T. V., Perchuk, L. L., & Burg, J.-P. (2008). Transient hot channels: Perpetrating and regurgitating ultrahigh-pressure, high-temperature crust–mantle associations in collision belts. *Lithos*, 103(1–2), 236–256. https://doi.org/10.1016/j.lithos.2007.09.017

Giese, J., Berger, A., Schreurs, G., & Gnos, E. (2011). The timing of the tectono-metamorphic evolution at the Neoproterozoic-Phanerozoic boundary in central southern Madagascar. *Precambrian Research*, 185, 131–148. https://doi.org/10.1016/j.precamres.2011.01.002

Grégoire, V., Nédélec, A., Monié, P., Montel, J.-M., Ganne, J., & Ralison, B. (2009). Structural reworking and heat transfer related to the late-Panafrican Angavo shear zone of Madagascar. *Tectonophysics*, 477(3–4), 197–216. https://doi.org/10.1016/j.tecto.2009.03.009

Hinojosa, J. H., & Mickus, K. L. (2002). Thermoelastic modeling of lithospheric uplift: A finite-difference numerical solution. *Computers & Geosciences*, 28(2), 155–167. https://doi.org/10.1016/S0098-3004(01)00028-0

Holder, R. M., & Hacker, B. R. (2019). Fluid-driven resetting of titanite following ultrahigh-temperature metamorphism in southern Madagascar. *Chemical Geology*, 504, 38–52. https://doi.org/10.1016/j.chemgeo.2018.11.017

Holder, R. M., Hacker, B. R., Horton, F., & Rakotondrazafy, A. M. (2018). Ultrahigh-temperature osumilite gneisses in southern Madagascar record combined heat advection and high rates of radiogenic heat production in a long-lived high-T orogen. *Journal of Metamorphic Geology*, 36(7), 855–880. https://doi.org/10.1111/jmg.12316

Holder, R. M., Sharp, Z. D., & Hacker, B. R. (2018). LinT, a simplified approach to oxygen-isotope thermometry and speedometry of high-grade rocks: An example from ultrahigh-temperature gneisses of southern Madagascar. *Geology*, 46(11), 931–934.

Holland, T. J. B., & Powell, R. (2011). An improved and extended internally consistent thermodynamic dataset for phases of

petrological interest, involving a new equation of state for solids. *Journal of Metamorphic Geology*, *29*(3), 333–383. https://doi.org/10.1111/j.1525-1314.2010.00923.x

Horstwood, M. S., Foster, G. L., Parrish, R. R., Noble, S. R., & Nowell, G. M. (2003). Common-Pb corrected in situ U–Pb accessory mineral geochronology by LA-MC-ICP-MS. *Journal of Analytical Atomic Spectrometry*, *18*(8), 837–846. https://doi.org/10.1039/B304365G

Horton, F., Hacker, B., Kylander-Clark, A., Holder, R., & Jöns, N. (2016). Focused radiogenic heating of middle crust caused ultrahigh temperatures in southern Madagascar. *Tectonics*, *35*(2), 293–314. https://doi.org/10.1002/2015TC004040

Jöns, N., & Schenk, V. (2011). The ultrahigh temperature granulites of southern Madagascar in a polymetamorphic context: Implications for the amalgamation of the Gondwana supercontinent. *European Journal of Mineralogy*, *23*, 127–156.

Kelley, S. P., & Wartho, J. A. (2000). Rapid kimberlite ascent and the significance of Ar-Ar ages in xenolith phlogopites. *Science*, *289*(5479), 609–611. https://doi.org/10.1126/science.289.5479.609

Kelsey, D. E., & Hand, M. (2015). On ultrahigh temperature crustal metamorphism: Phase equilibria, trace element thermometry, bulk composition, heat sources, timescales and tectonic settings. *Geoscience Frontiers*, *6*(3), 311–356. https://doi.org/10.1016/j.gsf.2014.09.006

Kohn, M. J., Penniston-Dorland, S. C., & Ferreira, J. C. (2016). Implications of near-rim compositional zoning in rutile for geothermometry, geospeedometry, and trace element equilibration. *Contributions to Mineralogy and Petrology*, *171*(10), 78. https://doi.org/10.1007/s00410-016-1285-1

Korhonen, F. J., Brown, M., Clark, C., & Bhattacharya, S. (2013). Osumilite–melt interactions in ultrahigh temperature granulites: Phase equilibria modelling and implications for the P–T–t evolution of the Eastern Ghats Province, I ndia. *Journal of Metamorphic Geology*, *31*(8), 881–907. https://doi.org/10.1111/jmg.12049

Košler, J., Sláma, J., Belousova, E., Corfu, F., Gehrels, G. E., Gerdes, A., Horstwood, M. S., Sircombe, K. N., Sylvester, P. J., & Tiepolo, M. (2013). U-Pb detrital zircon analysis—Results of an inter-laboratory comparison. *Geostandards and Geoanalytical Research*, *37*(3), 243–259. https://doi.org/10.1111/j.1751-908X.2013.00245.x

Kunz, B. E., Regis, D., & Engi, M. (2018). Zircon ages in granulite facies rocks: decoupling from geochemistry above 850 °C? *Contributions to Mineralogy and Petrology*, *173*(3). https://doi.org/10.1007/s00410-018-1454-5

Kylander-Clark, A. R. (2017). Petrochronology by laser-ablation inductively coupled plasma mass spectrometry. *Reviews in Mineralogy and Geochemistry*, *83*(1), 183–198. https://doi.org/10.2138/rmg.2017.83.6

Kylander-Clark, A. R. C., Hacker, B. R., & Cottle, J. M. (2013). Laser-ablation split-stream ICP petrochronology. *Chemical Geology*, *345*, 99–112. https://doi.org/10.1016/j.chemgeo.2013.02.019

Lexa, O., Schulmann, K., Janoušek, V., Štípská, P., Guy, A., & Racek, M. (2011). Heat sources and trigger mechanisms of exhumation of HP granulites in Variscan orogenic root. *Journal of Metamorphic Geology*, *29*(1), 79–102. https://doi.org/10.1111/j.1525-1314.2010.00906.x

Markl, G., Bäuerle, J., & Grujic, D. (2000). Metamorphic evolution of Pan-African granulite facies metapelites from Southern Madagascar. *Precambrian Research*, *102*(1), 47–68. https://doi.org/10.1016/S0301-9268(99)00099-6

Marschall, H. R., Dohmen, R., & Ludwig, T. (2013). Diffusion-induced fractionation of niobium and tantalum during continental crust formation. *Earth and Planetary Science Letters*, *375*, 361–371. https://doi.org/10.1016/j.epsl.2013.05.055

Martelat, J., Nicollet, C., Lardeaux, J., Vidal, G., & Rakotondrazafy, R. (1997). Lithospheric tectonic structures developed under high-grade metamorphism in the southern part of Madagascar. *Geodinamica ActaRevue de Geologie Dynamique et de Geographie Physique*, *10*(3), 94–114.

Martelat, J.-E., Cardon, H., Lardeaux, J.-M., Nicollet, C., Schulmann, K., & Pili, É. (2020). Geophysical evidences for large-scale mullion-type structures at the mantle–crust interface in southern Madagascar: Implications for Neoproterozoic orogeny. *International Journal of Earth Sciences*, *109*(4), 1487–1500. https://doi.org/10.1007/s00531-020-01840-w

Martelat, J.-E., Lardeaux, J.-M., Nicollet, C., & Rakotondrazafy, R. (2000). Strain pattern and late Precambrian deformation history in southern Madagascar. *Precambrian Research*, *102*(1), 1–20. https://doi.org/10.1016/S0301-9268(99)00083-2

Martelat, J.-E., Malamoud, K., Cordier, P., Randrianasolo, B., Schulmann, K., & Lardeaux, J.-M. (2012). Garnet crystal plasticity in the continental crust, new example from south Madagascar. *Journal of Metamorphic Geology*, *30*(4), 435–452. https://doi.org/10.1111/j.1525-1314.2012.00974.x

Martelat, J.-E., Randrianasolo, B., Schulmann, K., Lardeaux, J.-M., & Devidal, J.-L. (2014). Airborne magnetic data compared to petrology of crustal scale shear zones from southern Madagascar: A tool for deciphering magma and fluid transfer in orogenic crust. *Journal of African Earth Sciences*, *94*, 74–85. https://doi.org/10.1016/j.jafrearsci.2013.07.003

Martin, R. F., Randrianandraisana, A., & Boulvais, P. (2014). Ampandrandava and similar phlogopite deposits in southern Madagascar: Derivation from a silicocarbonatitic melt of crustal origin. *Journal of African Earth Sciences*, *94*, 111–118.

Montel, J.-M., Razafimahatratra, D., De Parseval, P., Poitrasson, F., Moine, B., Seydoux-Guillaume, A.-M., Pik, R., Arnaud, N., & Gibert, F. (2018). The giant monazite crystals from Manangotry (Madagascar). *Chemical Geology*, *484*, 36–50. https://doi.org/10.1016/j.chemgeo.2017.10.034

Moyen, J.-F. (2020). Granites and crustal heat budget. *Geological Society, London, Special Publications*, *491*(1), 77–100. https://doi.org/10.1144/SP491-2018-148

Paton, C., Hellstrom, J., Paul, B., Woodhead, J., & Hergt, J. (2011). Iolite: Freeware for the visualisation and processing of mass spectrometric data. *Journal of Analytical Atomic Spectrometry*, *26*(12), 2508. https://doi.org/10.1039/c1ja10172b

Paton, C., Woodhead, J. D., Hellstrom, J. C., Hergt, J. M., Greig, A., & Maas, R. (2010). Improved laser ablation U-Pb zircon geochronology through robust downhole fractionation correction. *Geochemistry, Geophysics, Geosystems*, *11*(3), 1–36. https://doi.org/10.1029/2009gc002618

Pattison, D. R. M., Chacko, T., Farquhar, J., & McFarlane, C. R. M. (2003). Temperatures of granulite-facies metamorphism: Constraints from experimental phase equilibria and thermobarometry corrected for retrograde exchange. *Journal*

of Petrology, 44(5), 867–900. https://doi.org/10.1093/petrology/44.5.867

Pattison, D. R. M., Chacko, T., Farquhar, J., McFarlane, C. R. M., & Widney, J. (2019). Program "RCLC": Garnet–orthopyroxene Thermobarometry corrected for late Fe–Mg exchange. Journal of Petrology, 60(5), 1107–1108. https://doi.org/10.1093/petrology/egz018

Pili, E., Sheppard, S. M., Lardeaux, J.-M., Martelat, J.-E., & Nicollet, C. (1997). Fluid flow vs. scale of shear zones in the lower continental crust and the granulite paradox. Geology, 25(1), 15–18. https://doi.org/10.1130/0091-7613(1997)025%3C0015:FFVSOS%3E2.3.CO;2

Popov, D. V., Spikings, R. A., Scaillet, S., O'Sullivan, G., Chew, D., Badenszki, E., Daly, J. S., Razakamanana, T., & Davies, J. H. (2020). Diffusion and fluid interaction in Itrongay pegmatite (Madagascar): Evidence from in situ $^{40}Ar/^{39}Ar$ dating of gem-quality alkali feldspar and UPb dating of protogenetic apatite inclusions. Chemical Geology, 556, 119841. https://doi.org/10.1016/j.chemgeo.2020.119841

Raith, M., Rakotondrazafy, R., & Sengupta, P. (2008). Petrology of corundum-spinel-sapphirine-anorthite rocks (sakenites) from the type locality in southern Madagascar. Journal of Metamorphic Geology, 26(6), 647–667. https://doi.org/10.1111/j.1525-1314.2008.00779.x

Rosenberg, C. L., & Handy, M. R. (2005). Experimental deformation of partially melted granite revisited: Implications for the continental crust. Journal of Metamorphic Geology, 23(1), 19–28. https://doi.org/10.1111/j.1525-1314.2005.00555.x

Rubatto, D. (2002). Zircon trace element geochemistry: Partitioning with garnet and the link between U–Pb ages and metamorphism. Chemical Geology, 184(1–2), 123–138. https://doi.org/10.1016/S0009-2541(01)00355-2

Štípská, P., Powell, R., Hacker, B. R., Holder, R., & Kylander-Clark, A. R. C. (2016). Uncoupled U/Pb and REE response in zircon during the transformation of eclogite to mafic and intermediate granulite (Blanský les, Bohemian Massif). Journal of Metamorphic Geology, 34(6), 551–572. https://doi.org/10.1111/jmg.12193

Spear, F. S., Kohn, M. J., & Cheney, J. T. (1999). P-T paths from anatectic pelites. Contributions to Mineralogy and Petrology, 134(1), 17–32. https://doi.org/10.1007/s004100050466

Stepanov, A. S., Hermann, J., Rubatto, D., & Rapp, R. P. (2012). Experimental study of monazite/melt partitioning with implications for the REE, Th and U geochemistry of crustal rocks. Chemical Geology, 300, 200–220.

Stern, R. J. (1994). Arc-assembly and continental collision in the Neoproterozoic African Orogen: Implications for the consolidation of Gondwanaland. Annual Review of Earth and Planetary Sciences, 22, 319–351. https://doi.org/10.1146/annurev.ea.22.050194.001535

Stüwe, K. (1998). Heat sources of Cretaceous metamorphism in the Eastern Alps — a discussion. Tectonophysics, 287(1-4), 251–269. https://doi.org/10.1016/s0040-1951(98)80072-3

Taylor, S. R., & McLennan, S. M. (1995). The geochemical evolution of the continental crust. Reviews of Geophysics, 33(2), 241–265. https://doi.org/10.1029/95RG00262

Thomas, J. B., Watson, E. B., Spear, F. S., Shemella, P. T., Nayak, S. K., & Lanzirotti, A. (2010). TitaniQ under pressure: The effect of pressure and temperature on the solubility of Ti in quartz. Contributions to Mineralogy and Petrology, 160(5), 743–759. https://doi.org/10.1007/s00410-010-0505-3

Thomas, J. B., Watson, E. B., Spear, F. S., & Wark, D. A. (2015). TitaniQ recrystallized: Experimental confirmation of the original Ti-in-quartz calibrations. Contributions to Mineralogy and Petrology, 169(3), 27. https://doi.org/10.1007/s00410-015-1120-0

Tucker, R. D., Roig, J. Y., Moine, B., Delor, C., & Peters, S. G. (2014). A geological synthesis of the Precambrian shield in Madagascar. Journal of African Earth Sciences, 94, 9–30. https://doi.org/10.1016/j.jafrearsci.2014.02.001

Tunini, L., Jiménez-Munt, I., Fernandez, M., Vergés, J., Villaseñor, A., Melchiorre, M., & Afonso, J. C. (2016). Geophysical-petrological model of the crust and upper mantle in the India-Eurasia collision zone. Tectonics, 35(7), 1642–1669.

White, R. W., & Powell, R. (2002). Melt loss and the preservation of granulite facies mineral assemblages. Journal of Metamorphic Geology, 20(7), 621–632.

White, R. W., Powell, R., & Halpin, J. A. (2004). Spatially-focussed melt formation in aluminous metapelites from Broken Hill, Australia. Journal of Metamorphic Geology, 22(9), 825–845.

White, R. W., Powell, R., Holland, T. J. B., Johnson, T. E., & Green, E. C. R. (2014). New mineral activity–composition relations for thermodynamic calculations in metapelitic systems. Journal of Metamorphic Geology, 32(3), 261–286. https://doi.org/10.1111/jmg.12071

White, R. W., Powell, R., & Johnson, T. E. (2014). The effect of Mn on mineral stability in metapelites revisited: New a–x relations for manganese-bearing minerals. Journal of Metamorphic Geology, 32(8), 809–828. https://doi.org/10.1111/jmg.12095

Yakymchuk, C. (2017). Behaviour of apatite during partial melting of metapelites and consequences for prograde suprasolidus monazite growth. Lithos, 274, 412–426.

SUPPORTING INFORMATION

Additional supporting information may be found online in the Supporting Information section at the end of this article.

Table S1: EPMA major element analyses of major phases.
Table S2: EPMA titanium in quartz results.
Table S3: EPMA zirconium in rutile results.
Table S4: Calculated bulk rock and melt-reintegrated rock compositions.
Table S5: Zircon LASS results.
Table S6: Monazite LASS results.
Table S7: Rutile U–Pb results.
Table S8: RCLC inputs with Fe^{3+}.
Table S9: RCLC inputs without Fe^{3+}.
Table S10: RCLC results with Fe^{3+}.
Table S11: RCLC results without Fe^{3+}.
Table S12: RCLC with and without biotite and cordierite.
Table S13: LASS parameters.

Figure S1: Comparison of published *P–T* estimates for southern Madagascar.

Figure S2: Effects of major element variability on thermobarometry.

Figure S3: Calculated mineral modes in *P–T* space.

Figure S4: Transects used for RCLC thermobarometry and the results of RCLC sensitivity tests.

Appendix S1: Python script for RCLC.

Appendix S2: Documentation for the RCLC python script